Nuclear Science and Techniques (2025) 36:143
https://doi.org/10.1007/s41365-025-01714-3

$^{12}C+^{12}C$ fusion reaction at astrophysical energies using HOPG target

Shuo Wang[1,2] · Yun-Zhen Li[2,3] · Long-Hui Ru[2] · Xin-Yu Wang[2,3] · Ning-Tao Zhang[2,3] · Yi-Hua Fan[2,3] · Yu-Cheng Feng[2] · Bing-Shui Gao[2,3] · Hao Huang[2,3] · Tao-Yu Jiao[2,3] · Hao Jian[2,3] · Kuo-Ang Li[2,3] · Jia-Qing Li[2,3] · Li-Bin Li[2] · Xiao-Bin Li[2,3] · Chen-Gui Lu[2,3] · En-Qiang Liu[2,3] · Bing-Feng Lv[2,3] · Hong-Yi Ma[2,3] · Hooi-Jin Ong[2,3] · Fu-Shuai Shi[2,3] · Liang-Ting Sun[2,3] · Xiao-Dong Tang[2,3] · Yu Tang[2,3] · Bing Wang[2] · Hou-Qing Wang[2] · Yao Yang[2,3] · Yu-Han Zhai[2,3] · Jin-Long Zhang[2,3] · Bo Zhang[2] · Peng Zhang[2] · Zhi-Chao Zhang[2,3] · Xiao-Dong Xu[2,3] · Wei-Ping Lin[1] · Chun Wen[1] · De-Hao Xie[1] · Zhi-Yong Zhang[4] · Xiao Fang[5] · Hong-Yi Wu[6] · Tao Tian[6] · Jun-Rui Ma[7] · Cheng-Lin Hao[8] · Yu-Na Yang[8] · Yu-Yang Yu[8] · Xue Liu[8] · Yun-Long Lu[8] · Si-Tao Zhu[8]

Received: 15 August 2024 / Revised: 4 November 2024 / Accepted: 15 November 2024 / Published online: 4 June 2025

Abstract
Highly oriented pyrolytic graphite (HOPG) is frequently adopted as the reaction target in $^{12}C+^{12}C$ fusion reaction experiments owing to its superior purity. In this study, we investigate the reaction yield dependence on the accumulated beam dose on HOPG target using a novel detection system consisting of a time-projection chamber and silicon array. The reaction yields are significantly reduced under intense beam bombardment owing to radiation damage to the HOPG surface. The α_0 and $p_{0,1}$ yields decrease by 51.5% and 25%, respectively, when the $^{12}C^{2+}$ beam dose accumulates at 5 C. Using the novel detection system and HOPG target, the α_0 yield is determined to be $2.68^{+4.69}_{-1.69}\times10^{-17}/^{12}C$ after correcting for the yield loss due to radiation damage. Our result represents the highest sensitivity achieved to date in direct measurements of $^{12}C(^{12}C,\alpha_0)^{20}Ne$.

Keywords Massive star · Fusion reaction · Projection chamber · Low background

1 Introduction

Carbon fusion is the primary reaction in massive stars [1–4]. It also serves as an ignition reaction for Type Ia supernova explosions [5, 6] and X-ray superbursts [7, 8]. An accurate carbon–carbon fusion reaction rate can reduce uncertainties in the nucleosynthesis of massive stars and the ignition condition in Type Ia supernova as well as contribute to resolving the ignition problem in superbursts [9, 10].

This work was supported by the Strategic Priority Research Program of the Chinese Academy of Sciences (No. XDB34020200), National Key Research and Development Program (MOST 2022YFA1602304), Scientific Research Instrument and Equipment Development Program of the Chinese Academy of Sciences (No. GJJSTD20210007), and National Natural Science Foundation of China (Nos. 12175156, U1632142).

✉ Ning-Tao Zhang
zhangningtao@impcas.ac.cn

✉ Wei-Ping Lin
linwp1204@scu.edu.cn

[1] Key Laboratory of Radiation Physics and Technology of the Ministry of Education, Institute of Nuclear Science and Technology, Sichuan University, Chengdu 610064, China

[2] Institute of Modern Physics, Chinese Academy of Sciences, Lanzhou 730000, China

[3] School of Nuclear Science and Technology, University of Chinese Academy of Sciences, Beijing 00049, China

[4] University of Science and Technology of China, Hefei 230026, China

[5] Sino-French Institute of Nuclear Engineering and Technology, Sun Yat-sen University, Zhuhai 519082, Guangdong, China

[6] Key Laboratory of Nuclear Data, China Institute of Atomic Energy, Beijing 102413, China

[7] Southern University of Science and Technology, Shenzhen 518055, Guangdong, China

[8] Beijing Normal University, Beijing 100875, China

The carbon–carbon fusion reaction in stars occurs at energies below $E_{c.m.}$= 3.0 MeV, which is considerably below the Coulomb barrier at $E_{c.m.}$ ≈ 5.8 MeV [11, 12], resulting in an extremely low fusion cross section. For example, the fusion cross section at $E_{c.m.}$= 2.0 MeV was estimated to be 0.1 pb based on the CF88 recommendation [13]. At $E_{c.m.}$ < 3.0 MeV, the dominant exit channels are the alpha and proton channels, whereas the neutron channel is closed at its threshold of $E_{c.m.}$= 2.597 MeV [14, 15]. Previous measurements relied on detecting light charged particles [16–19] or gamma rays emitted by residual nuclei [20, 21]. Recently, a particle-gamma coincidence method was developed to further suppress background noise and achieve better measurements at stellar energies [22, 23]. LUNA-MV is planned to study the ^{12}C+^{12}C reaction by detecting the 440 keV and 1634 keV gamma rays emitted by the proton and alpha channels, respectively, in the Gran Sasso underground laboratory, where natural and cosmic-ray-induced gamma backgrounds are considerably reduced [24]. JUNA, in China, also demonstrates the potential to suppress background noise [25–28].

Although the particle-gamma coincidence method and underground gamma-ray measurements can extend the measurement to even lower energies, the channels of charged particles decaying to the ground states of ^{23}Na and ^{20}Ne cannot be studied using these methods owing to the absence of gamma rays [18, 29]. We developed a novel technique based on a time-projection chamber (TPC) to measure the non-gamma-ray-emitting channels ^{12}C(^{12}C,α_0)^{20}Ne and ^{12}C(^{12}C,p_0)^{23}Na. Our commissioning experiment using the 1024-channel prototype pMATE TPC (multi-purpose time-projection chamber for nuclear astrophysical and exotic-beam experiments) demonstrated that more than 99% of alpha contaminants from the natural environment may be rejected by this technique [30].

An ultrapure carbon target able to withstand beam powers exceeding 400 W is another important factor in carbon fusion experiments [31, 32]. The background induced by the target impurities, primarily hydrogen and lithium isotopes, may be orders of magnitude higher than the reaction events of interest, limiting the experimental sensitivities. Therefore, obtaining high-purity carbon targets is important to achieve the desired sensitivity. In addition, the small ^{12}C+^{12}C fusion reaction cross section at stellar energies requires high beam intensity and a long beam time on the order of weeks. Therefore, target stability is another important feature of carbon targets.

This study reports the first direct measurement of the ^{12}C(^{12}C,α_0)^{20}Ne reaction at $E_{c.m.}$= 2.22 MeV using the highly oriented pyrolytic graphite (HOPG) target and our upgraded TPC-Si detector array. We also investigate the impact of radiation damage on the detected yield of charged particles such as protons and alpha particles. This study consists of four parts. The first part introduces the experimental setup. The second part describes the experimental method. The third part reports the study of the dependence of the detected yield of charged particles on the accumulated dose of the HOPG target. In the fourth part, we present the measurement of the thick target yield of ^{12}C(^{12}C,α_0)^{20}Ne at $E_{c.m.}$= 2.22 MeV using the HOPG target.

2 Experimental setup

The experimental setup comprises a reaction chamber and detector chamber. A schematic of the setup is shown in Fig. 1. In the reaction chamber, a thick carbon target was mounted on water-cooled stainless-steel backing. The angle between the beam and normal directions of the target surface was set to 135°, allowing the light charged particles from the fusion reaction to be detected by the detectors. A water-cooled collimator with a diameter of 10 mm was installed 40 cm upstream of the target, and the beam spot on the target was limited to ~10 mm.

Our detection system comprises a TPC and silicon detector array. It was installed in the detector chamber filled with counting gas. A large-area Kapton foil with a thickness of 5 μm and an area of 7 cm × 21 cm was used to separate the gas in the detector chamber from the reaction chamber. The Kapton foil was coated with approximately 100-nm-thick aluminum to prevent charge accumulation and shield the silicon detectors from light coming from the beam spot on the carbon target. Two types of stainless-steel hexagonal meshes with transmittances of 77% and 90% were used to support the foil; the typical gas pressure varied from 50 to 300 mbar.

The TPC has an active volume of 100 mm (W) × 200 mm (L) × 200 mm (H). When the charged

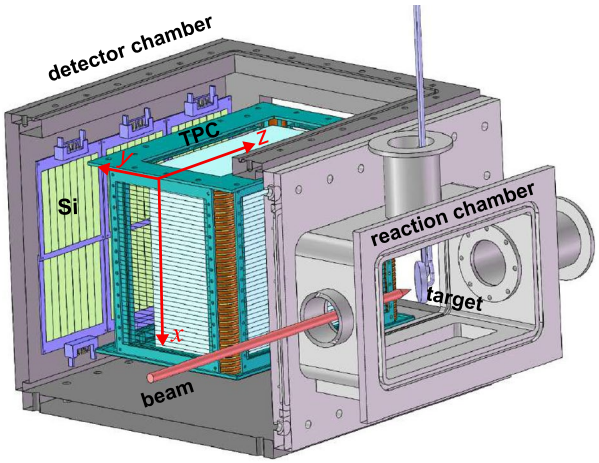

Fig. 1 (Color online) Schematic of the experimental setup. In the coordinate system defined in the setup, the target position is deduced to be (10 cm, −21 cm, 10 cm)

particles travel in the TPC gas region, they ionize the gas along their paths. The ionized electrons drift along the electric field toward the anode-readout plate, and an avalanche occurs. The primary and avalanche electrons are collected using an anode plate with rectangular pads.

The three-dimensional position can be determined by measuring the electron drift time. Further details of the TPC detector and its commissioning experiment are provided in Ref. [30, 33].

The silicon array consists of six silicon detectors (Hamamatsu, Japan) with thicknesses of 600 µm [34]. Each silicon detector has eight strips at the junction side in a direction parallel to the electric field of the TPC, dividing the scattering angle into a finer size. The total active area is 90.6 mm × 90.6 mm. The distance between the silicon array and TPC active region can be adjusted from 80 mm to 120 mm. The combination of the silicon detectors and TPC forms a $DE-E$ telescope system. In addition, silicon detectors can provide a starting point for measuring the drift time of electrons in the TPC.

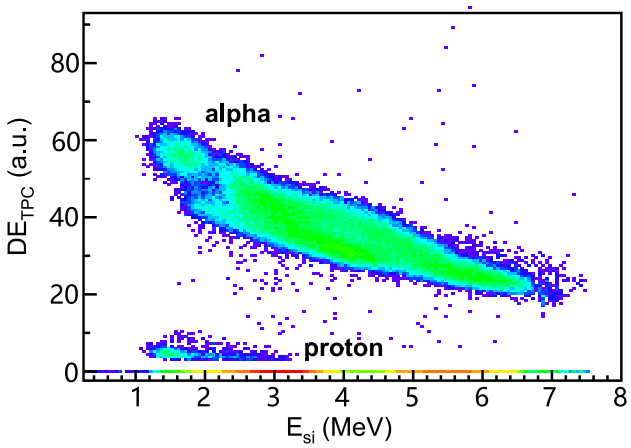

Fig. 2 (Color online) Particle identification using the energy loss in TPC versus the energy in silicon detectors for the $^{12}C+^{12}C$ fusion reaction at E_{lab}= 7.8 MeV. The detector was placed at 90° with a pressure of 135 mbar. GEM-based readout pads were used. The TPC was optimized for alpha detection, whereas most protons were only recorded by the silicon detectors. The discontinuity in the alpha band around 2 MeV by Si was caused by the energy truncation in the middle silicon detectors, which had a relatively high-energy threshold (see Fig.4)

3 Experiments

A 2-mm-thick HOPG target was bombarded by the ^{12}C beam delivered by the low-energy high-intensity high-charge-state ion accelerator facility at the Institute of Modern Physics [35]. During the experiments presented in Sects.3 and 5, thick gas electron multipliers [36] were used for gas amplification, and the TPC chamber was placed at a scattering angle of 90°. To study the reaction yield variations using the HOPG target (Sect. IV), the TPC with MicroMegas amplification was used for stable operation at a low gas pressure [37, 38] and was placed at a scattering angle of 120°. The gas type and pressure were selected to ensure that the charged particles could penetrate the TPC active volume and stop in the Si detectors while depositing sufficient energy in the gas to generate tracks.

A typical DE_{TPC}-E_{si} spectrum measured at $E_{c.m.}$= 3.90 MeV is shown in Fig. 2. Here, DE_{TPC} and E_{si} are the energy depositions in the TPC and Si detectors, respectively. The TPC chamber was filled with a He+5% CO_2 mixture at 165 mbar. With the energy loss in the TPC and residual energy in the silicon detectors, alpha events were well separated from protons and other events, as shown in Fig. 2. During this measurement, the TPC gain was optimized for the detection of alpha particles, whereas protons with energies above 3 MeV did not generate tracks in the TPC.

An important advantage of the TPC is its ability to track charged particles [30, 39]. The tracks of the alpha events can be traced back to the beam axis to check whether they originated from the beam spot on the reaction target. An example of track reconstruction in the pad plane (YZ plane)

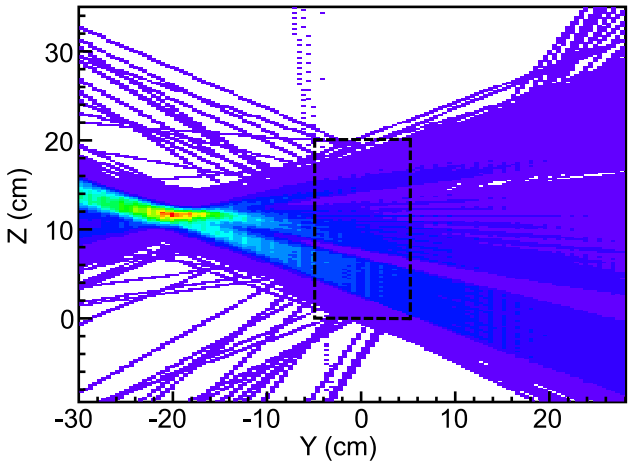

Fig. 3 (Color online) Accumulation of extended alpha tracks in the pad plane for the target reconstruction. TPC active region is indicated by the black dashed line in the plot. Most of the tracks converged to the reaction target position, which has a diameter of approximately 7 mm. The experimental setup is explained in the caption of Fig. 2

using the selected alpha events is shown in Fig. 3. Most tracks converged around the (−20 cm, 11 cm) point, which clearly defined the beam spot on the reaction target. All other events mostly originated from the natural radioactivity of the surrounding material. The alpha events from the beam spot could be further purified using the TPC drift time [30].

The alpha particles emitted from the target position were selected by gating their DE_{TPC}, E_{si}, and tracks were detected

by the TPC. The energy-deposition spectrum in the silicon detectors as a function of strip ID, which corresponds to the polar angle relative to the beam axis, is shown in Fig. 4. The two groups of alpha particles shown in Fig. 4, corresponding to the ground and first excited states of the residual nucleus ^{20}Ne, are identified with their kinematics. The relatively large energy spread of the alpha particles mainly resulted from the combined effects of kinematic broadening, energy loss, and straggling in the thick carbon target, Kapton window, and counting gas.

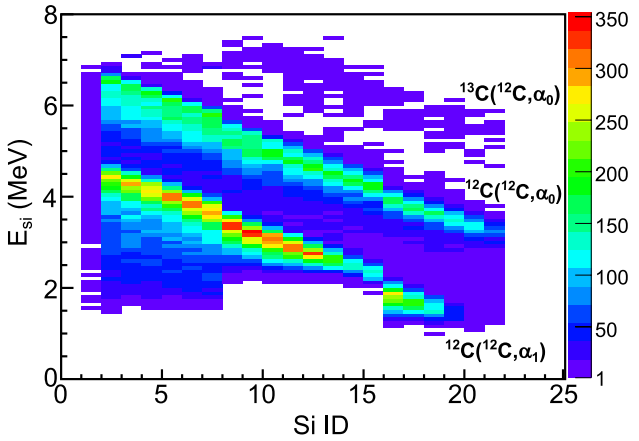

Fig. 4 (Color online) Energy measured in silicon detectors versus the silicon-strip number, obtained from a graphical representation of alpha events in the $DE_{\mathrm{TPC}} - E_{\mathrm{si}}$ matrix in Fig. 2. Silicon IDs from 0 to 23 correspond to the scattering angles of 70° to 110° in the laboratory frame. The ^{13}C(^{12}C,α)^{20}Ne reaction events are also observed, in which the ^{13}C nucleus comes from the natural abundance of 1.1% in the HOPG target. The experimental setup is explained in the caption of Fig. 2

4 Stability of the HOPG target

The HOPG target was composed of several graphene layers. After beam bombardment, the graphene layers on the surface were damaged and formed a flaky and wrinkled structure as shown in Fig. 5. This radiation damage modified the surface structure and may potentially affect the detection of low-energy charged particles, a phenomenon that has not yet been studied.

We studied the effect of intense beam irradiation on the HOPG target by measuring ^{12}C+^{12}C reaction yields. In the test, a $^{12}C^{2+}$ beam at a relatively high energy of $E_{\mathrm{c.m.}}$= 3.55 MeV was chosen to obtain sufficient statistics within a few minutes. The detector was placed at an angle of 120° at a gas pressure of 99 mbar. During charge accumulation, the beam was $^{12}C^{2+}$ with a typical current of 40 ~ 50 pμA. Two types of targets, 4-μm-thick diamond-like carbon (DLC) [40] and 2-mm-thick HOPG targets [41], were used to study the variations in the yields of the carbon–carbon fusion reaction as a function of the beam dose.

Fig. 5 (Color online) Picture of HOPG target before (left) and after 1.34×10^7 μC beam dose bombardment (right)

An infrared camera was used to monitor the maximum temperature of the target. The observations indicate that the beam spot size on the DLC and HOPG was approximately 1 cm^2. With water cooling at the back of the target, the maximum temperature of the DLC surface stabilized at approximately 100 °C. However, the surface temperature of the HOPG target quickly increased to ~400 °C when the beam hit it. This difference might have been caused by the weak interlayer interactions between the individual graphene layers in the HOPG target [41, 42]. Such a structure led to a low through-plane thermal conductivity, which was more than two orders of magnitude lower than that of natural graphite. The formation of flaky and wrinkled structures after irradiation further reduced thermal conduction.

During measurements, the TPC was placed at 120°. The detector chamber was filled with a gas mixture of 90% He, 5% CO_2, and 5% Ar at a pressure of 100 mbar. As discussed in the previous section, the alpha yield was determined directly by selecting the alpha band in the $DE_{\mathrm{TPC}} - E_{\mathrm{si}}$ condition and the tracking information. Protons can be selected by applying an anti-alpha condition, which excludes alpha events from the $DE_{\mathrm{TPC}} - E_{\mathrm{si}}$ spectrum.

4.1 *Q*-value spectra of the alpha and proton channels

The reaction Q values for the proton ($Q_{\mathrm{g.s.}}$= 2.24 MeV) and alpha ($Q_{\mathrm{g.s.}}$= 4.62 MeV) channels were calculated using the following formulas:

$$Q = \left(\frac{A_a}{A_B} - 1\right)E_a + \left(\frac{A_b}{A_B} + 1\right)E_b - \frac{2\sqrt{A_a A_b E_a E_b}\cos\theta}{A_b}, \quad (1)$$

where A_a, A_b, and A_B are the mass numbers of the projectile, ejected, and residual nuclei, respectively. E_a is the kinetic energy of the projectile during the reaction, E_b is the energy of the ejected light particles, and θ is the scattering angle of

particle b. E_b is obtained using the energy detected by the silicon detector and energy losses in the entrance window and gas region [43].

To reduce the systematic error arising from energy loss correction, only the events measured by the two silicon detectors in the middle were used.

The Q-value spectra of ^{12}C(^{12}C,α)^{20}Ne and ^{12}C(^{12}C,p)^{23}Na at $E_{\mathrm{c.m.}}$= 3.55 MeV are shown in Fig. 6 and 7, respectively. The green line in Fig. 6 shows the Q-value spectrum for ^{12}C(^{12}C,α)^{20}Ne using the DLC target at a beam charge of 2.18×10^4 μC. This spectrum was measured at the beginning of the beam irradiation. The α_0 and α_1 peaks were located at Q values of 4.62 MeV and 2.99 MeV, respectively. No noticeable change was observed in the Q-value spectrum during the subsequent charge accumulation on the DLC.

The black and blue lines shown in Fig. 6 represent the HOPG target with the accumulated charges of 4.82×10^4 μC and 4.94×10^6 μC, respectively. Comparing the shapes of the Q-value spectra of the HOPG and DLC targets, we can clearly observe a shift and broadening of the α_0 and α_1 peaks for HOPG as the beam dose increases. The black and blue lines shown in Fig. 7 represent the Q-value spectra for protons corresponding to 2.59×10^5 μC and 4.94×10^6 μC on the HOPG, respectively. The p_0 and p_1 peaks are located at Q values of 2.24 MeV and 1.80 MeV, respectively. The p_0 and p_1 peaks become broader and develop a longer tail toward the lower Q-value region after approximately 5 C of radiation.

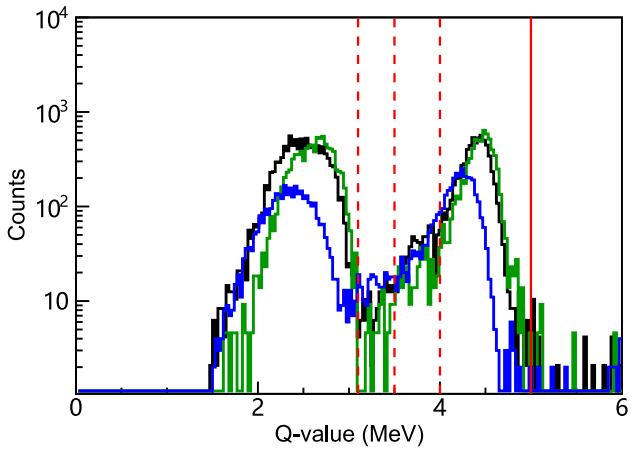

Fig. 6 (Color online) Q-value spectrum for ^{12}C(^{12}C,α)^{20}Ne obtained with different cumulative charge at $E_{\mathrm{c.m.}}$= 3.55 MeV. The histograms in black and blue represent the Q-value spectra for HOPG with cumulative charges of 4.82×10^4 μC and 4.94×10^6 μC, respectively. The Q-value spectrum for DLC at 2.18×10^4 μC is also plotted for comparison (green line). The vertical solid line indicates the upper limit (5.0 MeV) of integration in calculating the α_0 yield, whereas the three dashed lines correspond to the lower limits (3.1, 3.5, and 4.0 MeV) in different integrations (see Fig. 8 for comparisons of the integrated yields)

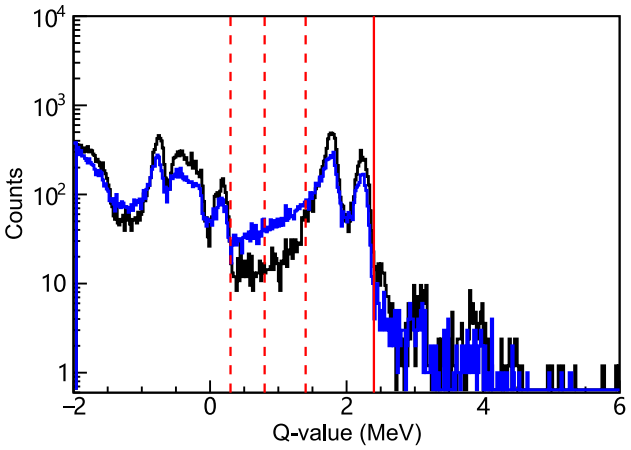

Fig. 7 (Color online) Q-value spectrum for ^{12}C(^{12}C,p)^{23}Na at $E_{\mathrm{c.m.}}$= 3.55 MeV. The black and blue histograms represent the Q-value spectra for HOPG at 2.59×10^5 μC and 4.94×10^6 μC, respectively. The vertical solid line indicates the upper integral limit (2.4 MeV) when calculating the p_0+p_1 yield, whereas the three dashed lines correspond to the lower limits (0.3, 0.8, and 1.4 MeV) in different integrations (see Fig. 9 for comparisons of the integrated yields)

4.2 Dependence of the measured alpha and proton yields on the beam dose

We investigated the dependence of the measured alpha and proton yields on the beam dose. The reaction yields were calculated by integrating the peaks of the protons and alpha particles in the Q-value spectra divided by the incident-beam particles.

The yield variations in α_0 and $p_0 + p_1$ are presented in Fig. 8 and 9, respectively, as a function of accumulated charge. For each channel, three different yields corresponding to different integral ranges in the Q-value spectra (indicated by red lines in Fig. 6 and 7) were obtained to account for the change in the Q-value spectra. With an increase in the charge on the HOPG, the yields of both α_0 and $p_0 + p_1$ exhibited a notable decrease. This scenario worsened for the alpha-emission channels. The decreasing trend in the yield of α_0 (4.0 MeV < Q-value < 5.0 MeV) for HOPG can be fitted well by the following exponential function:

$$\mathrm{Yield}(/^{12}\mathrm{C}) = \exp(-26.68 - 1.47 \times 10^{-7} \times \mathrm{charge}/\mu\mathrm{C}). \quad (2)$$

Based on the fitted yield curves shown in Fig. 8, the yield of α_0 decreased by 34.9% when the dose reached 3.0×10^6 μC and by 51.5% when the dose reached 5.0×10^6 μC. To mitigate the broadening effect induced by beam irradiation, we employed two extended integral ranges: [3.5 MeV, 5.0 MeV] and [3.1 MeV, 5.0 MeV]. Compared with the integration within [4.0 MeV, 5.0 MeV], the alpha yields increased by 22.0(0.8)% and 28(1)%, respectively, when the dose reached 4.94×10^6 μC. The α_0 yield obtained from the three integral

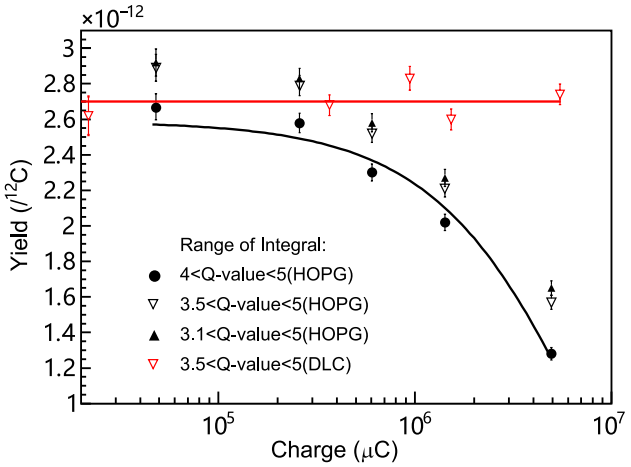

Fig. 8 (Color online) Yield of $^{12}C(^{12}C,\alpha_0)^{20}Ne$ versus the accumulated charge at $E_{c.m.}$=3.55 MeV. The three sets of labels represent the yields in the HOPG target using different Q-value integral intervals. The black solid curve represents the fitted yield curve for the HOPG within the Q-value-integral interval of [4.0 MeV, 5.0 MeV]. The red triangle represents the yield of the DLC (3 MeV< Q-value<5 MeV), and the red solid line is the fitted yield line (constant) with a mean value of 2.70×10^{-12} /^{12}C

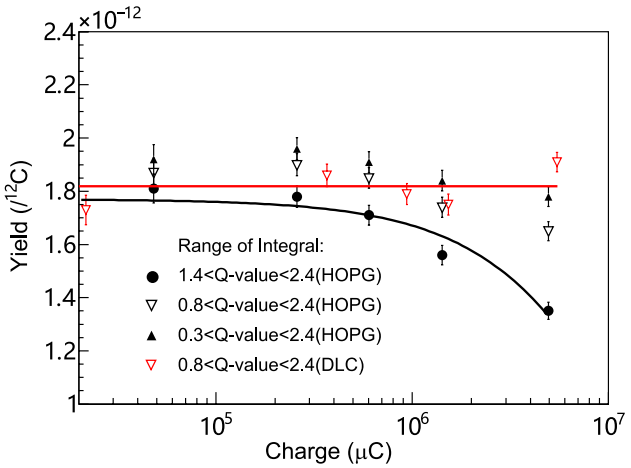

Fig. 9 (Color online) Yields of p_0+p_1 for $^{12}C(^{12}C,p)^{23}Na$ versus the accumulated charge at $E_{c.m.}$= 3.55 MeV. Three sets of different labels represent the yields of HOPG at different integral intervals. The red triangle represents the yield of DLC within the Q-value integral interval [0.8 MeV, 2.4 MeV], and the red line is the fitted yield line (constant) with a mean value of 1.82×10^{-12} /^{12}C. The black solid curve represents the fitted yield curve (1.4 MeV< Q-value < 2.4 MeV) by the exponential function: Yield(/^{12}C) = $\exp(-27.06 - 5.76\times10^{-8}\times$ charge/μC)

ranges exhibited a similar trend as the accumulated charge increased from 0 C to ~5 C.

For comparison, the same test was performed using the DLC target. The maximum beam dose reached 5.5×10^6 μC. The yield of α_0 was approximately constant at 2.70×10^{-12} /^{12}C according to the fitted yield line, as shown in Fig. 8.

The DLC target contained a fraction of hydrogen. The yield difference for the DLC and HOPG targets at a nearly zero dose could be explained by the difference in stopping power.

Regarding the p_0+p_1 yield, the situation differed slightly. When the beam charge accumulated up to 5.0×10^6 μC, the yield decreased by 25% according to the fitted yield curve shown in Fig. 9. The decrease in the p_0+p_1 yield could be reduced to 7.0(0.3)% if the integration range is increased to [0.3 MeV, 2.4 MeV].

4.2.1 Discussion

Based on the above analysis, the $^{12}C(^{12}C,\alpha_0)^{20}Ne$ reaction yield in the HOPG target was significantly reduced under intense beam bombardment. The HOPG target surface was damaged and formed a flaky and wrinkled structure, whereas deeper HOPG layers were exposed to incident-beam particles. Some alpha particles from the fusion reaction were either stopped in the target or experienced more energy loss before escaping from the target surface, owing to the flaky and wrinkled structure. Consequently, the detected alpha Q-value spectrum was distorted and the integrated yield decreased as the beam dose increased.

Protons have better penetration power than alpha particles. For example, the stopping range of a 4-MeV proton in graphite materials is approximately 10 times longer than that of an α particle with the same energy [44]. This may be why the loss of the proton-reaction yield is less significant than that of the α particle. By increasing the integration limit in the Q-value spectrum, the effect on the proton-reaction yield was reduced to less than 10%, as shown in Fig. 9.

Notably, radiation damage is a very complex and combined process, depending not only on charge accumulation, but also on the areal power density, target cooling, and alpha energy. Very recently, Tan et al. discussed the dependence of radiation damage on beam energy [45]. Therefore, the fitted curve obtained in this study can only be applied to correct the yield obtained under conditions identical to our setup.

5 Measurement of $^{12}C(^{12}C,\alpha_0)^{20}Ne$ at $E_{c.m.}$= 2.22 MeV

We also measured the $^{12}C(^{12}C,\alpha)^{20}Ne$ reaction at $E_{c.m.}$= 2.22 MeV using the HOPG target to test the target purity and sensitivity of the TPC-detection technique. The cross section at this energy was estimated to be only a few tens of picobarns, based on the extrapolation of CF88 [11, 13]. The

$^{12}C^{4+}$ beam intensity was approximately 15 pμA, and the total accumulated charge was 3.26×10^6 μC. The detector was placed at 90 degrees and filled with 95%He+5%CO_2. Thick GEM-based readout pads were used. For the detection of α particles, the gas pressure in the TPC was optimized to 135 mbar.

Using the same analysis procedure, we obtained the spectrum of the energy deposited in the silicon detectors versus the silicon-strip number for the alpha events. The results are shown in Fig. 10; the top figure is obtained by gating the alpha events in the $DE_{TPC} - E_{si}$ spectrum through a 15-h run with the beam, and the bottom figure is obtained by gating the alpha events in the $DE_{TPC} - E_{si}$ spectrum and tracks originating from the beam spot. The difference between the two figures demonstrates the effectiveness of the proposed tracking technique. One α event was identified as originating from the $^{12}C(^{12}C,\alpha_0)^{20}Ne$ channel, with the aid of the kinematic curve calculated using the beam energy at the target surface. A total of 570 alpha events from the $^{13}C(d,\alpha)^{11}B$ reaction were also identified, as shown at the bottom of Fig. 10. The high-energy fronts of these events matched well with the expected kinematic curve calculated for the reaction occurring on the surface. A small number of DH^+ molecular ions could be mixed with the $^{12}C^{4+}$ beam and reacted with ^{13}C in the HOPG target. This group disappeared in our later measurements when we switched the charge state of the carbon beam from 4^+ to 2^+. Although these events contaminated the region of interest for the $^{12}C(^{12}C,\alpha_1)^{20}Ne$ channel, they provided valuable information about the beam spot for rejecting natural alpha radioactivity. The natural background of the detector setup was also investigated over a 98-h run without a beam, and the results are shown in Fig. 11. After applying the same cuts to the $^{12}C+^{12}C$ measurement, only one α event was observed outside the energy region of interest. As a result, we estimated zero α background counts during the 15-h in-beam measurement. By assuming an isotropic angular distribution in the center-of-mass frame, the

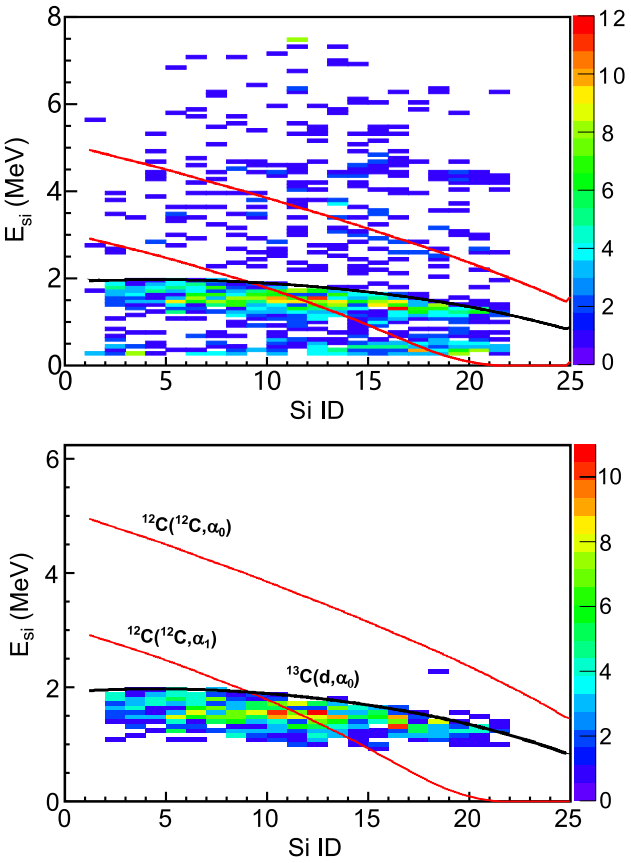

Fig. 10 (Color online) E_{si} versus the silicon-ID matrix for alpha particles from the $^{12}C+^{12}C$ measurement at $E_{c.m.}$=2.22 MeV. Silicon IDs from 0 to 23 correspond to scattering angles of 70–110 degrees in the laboratory frame. The original spectrum (top) and the spectrum obtained after choosing particles coming from the target position (bottom) show one alpha event (marked by the shaded zone), which is assigned to the $^{12}C(^{12}C,\alpha_0)^{20}Ne$ reaction based on the kinematic calculation (red solid line). Many alpha particles from the $^{13}C(d,\alpha)^{11}B$ reaction are also observed because a small amount of DH^+ ions are transported with the $^{12}C^{4+}$ beam. This is consistent with the calculated black line

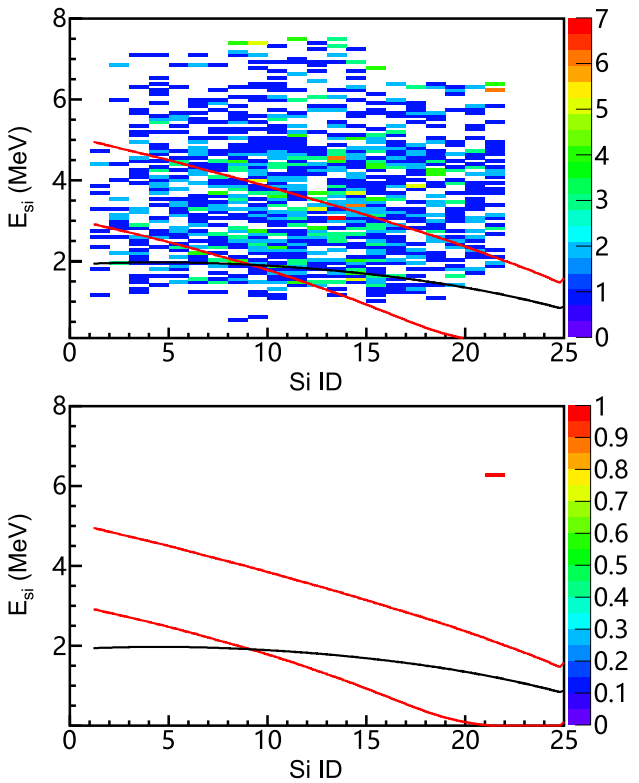

Fig. 11 (Color online) E_{si} versus the silicon-ID matrix for alpha particles from the natural background measurement. The original spectrum (top) and the spectrum obtained after choosing particles coming from the target position (bottom) show only one α event outside of the energy region of interest

thick-target yield for the $^{12}C(^{12}C,\alpha)^{20}Ne$ channel was deduced to be $1.68^{+2.94}_{-1.06}\times10^{-17}/^{12}C$. Error analysis followed the methodology outlined in Ref. [46]. Considering the effect of the accumulated charge on the HOPG target, the real thick-target yield was $2.68^{+4.69}_{-1.69}\times10^{-17}/^{12}C$ after correction, based on the fitted yield curve in Fig. 8. Our result represents the highest sensitivity achieved to date in direct measurements of $^{12}C(^{12}C,\alpha_0)^{20}Ne$.

6 Conclusion

Ultrapure high-power carbon targets are essential for experimental studies of $^{12}C+^{12}C$ fusion reactions at stellar energies. HOPG has frequently been adopted as a reaction target in experiments because of its superior purity. In this study, we investigated the reaction yield dependence on the accumulated beam dose on an HOPG target. Our results showed that the alpha yields were significantly reduced under intense beam bombardment. When the beam dose accumulated to 5 C, the decrease in the alpha yields was 51.5%. Moreover, shifts and broadening of the proton and alpha peaks were clearly observed. To obtain the absolute yield, a correction was required according to the beam dose on the target. Using the TPC-detection technique and HOPG target, we successfully extended the direct measurement of $^{12}C(^{12}C,\alpha_0)^{20}Ne$ to $E_{c.m.}$= 2.22 MeV, which is within the Gamow window for the carbon burning of massive stars. The thick target yield was determined to be $2.68^{+4.69}_{-1.69}\times10^{-17}/^{12}C$, representing the best sensitivity achieved to date for the direct measurement of $^{12}C(^{12}C,\alpha)^{20}Ne$. Further extension to lower energies requires further contaminant reduction in the target and more stable target materials capable of sustaining high beam intensities.

Author Contributions All authors contributed to the study conception and design. Material preparation, data collection, and analysis were performed by Shuo Wang, Yun-Zhen Li, Long-Hui Ru, Ning-Tao Zhang, Yu-Cheng Feng, Bing-Shui Gao, Hao Huang, Tao-Yu Jiao, Hao Jian, Kuo-Ang Li, Jia-Qing Li, Li-Bin Li, Xiao-Bin Li, Chen-Gui, Lu, En-Qiang Liu, Bing-Feng Lv, Hong-Yi Ma, Hooi-Jin Ong, Fu-Shuai Shi, Liang-Ting Sun, Xiao-Dong Tang, Yu Tang, Bing Wang, Hou-Qing Wang, Yao Yang, Yu-Han Zhai, Jin-Long Zhang, Bo Zhang, Peng Zhang, Zhi-Chao Zhang, Xiao-Dong Xu, Wei-Ping Lin, Chun Wen, De-Hao Xie, Zhi-Yong Zhang, Xiao Fang, Hong-Yi Wu, Tao Tian, Jun-Rui Ma, Cheng-Lin Hao, Yu-Na Yang, Yu-Yang Yu, Xue Liu, Yun-Long Lu, and Si-Tao Zhu. The first draft of the manuscript was written by Shuo Wang, Ning-Tao Zhang, Xiao-Dong Tang, Yun-Zhen Li, Wei-Ping Lin, and all authors commented on previous versions of the manuscript. All authors read and approved the final manuscript.

Data Availability The data that support the findings of this study are openly available in Science Data Bank at https://cstr.cn/31253.11.sciencedb.j00186.00630 and https://www.doi.org/10.57760/sciencedb.j00186.00630.

Declarations

Conflict of interest The authors declare that they have no conflict of interest.

References

1. C.E. Rolfs, W.S. Rodney, *Cauldrons in the Cosmos: Nuclear Astrophysics* (University of Chicago Press, Chicago, 1988)
2. X.D. Tang, Heavy ion fusion reactions in stars. AIP Conf. Proc. **1947**, 020024 (2022). https://doi.org/10.1063/1.5030828/14155008
3. X.D. Tang, L.H. Ru, The $^{12}C+^{12}C$ fusion reaction at stellar energies. AIP Conf. Proc. **260**, 01002 (2022). https://doi.org/10.1051/epjconf/202226001002
4. W.Y. Xin, K. Nomoto, G. Zhao et al., Impact of the new $^{12}C+^{12}C$ reaction rate on presupernova nucleosynthesis. Chin. Phys. C **47**, 034107 (2023). https://doi.org/10.1088/1674-1137/aca1ff
5. W. Hillebrandt, J.C. Niemeyer, Type Ia supernova explosion models. Annu. Rev. Astron. Astr. **38**, 191–230 (2000). https://doi.org/10.1146/annurev.astro.38.1.191
6. T. Kajino, Underground laboratory JUNA shedding light on stellar nucleosynthesis. Nucl. Sci. Tech. **34**, 42 (2023). https://doi.org/10.1007/s41365-023-01196-1
7. E.F. Brown, Nuclear heating and melted layers in the inner crust of an accreting neutron star. Astrophys. J. **531**, 988 (2000). https://doi.org/10.1086/308487
8. E.F. Brown, Superburst ignition and implications for neutron star interiors. Astrophys. J. **614**, L57 (2004). https://doi.org/10.1086/425562
9. R.L. Cooper, A.W. Steiner, E.F. Brown, Possible resonances in the $^{12}C + ^{12}C$ fusion rate and superburst ignitio. Astrophys. J. **702**, 660–671 (2009). https://doi.org/10.1088/0004-637X/702/1/660
10. L.R. Gasques, E.F. Brown, A. Chieffi et al., Implications of low-energy fusion hindrance on stellar burning and nucleosynthesis. Phys. Rev. C **76**, 035820 (2007). https://doi.org/10.1103/PhysRevC.76.035802
11. M. Pignatari, R. Hirschi, M. Wiescher et al., The $^{12}C+^{12}C$ reaction and the impact in nucleosynthesis in massive stars. Phys. Rev. C **762**, 31 (2013). https://doi.org/10.1088/0004-637X/762/1/31
12. M. Notani, H. Esbensen, X. Fang et al., Correlation between the $^{12}C+^{12}C$, $^{12}C+^{13}C$, and $^{13}C+^{13}C$ fusion cross sections. Phys. Rev. C **85**, 014607 (2012). https://doi.org/10.1103/PhysRevC.85.014607
13. G.R. Caughlan, W.A. Fowler, Thermonuclear reaction rates V. Atom. Data Nucl. Data. **40**, 283–334 (1988). https://doi.org/10.1016/0092-640X(88)90009-5
14. Y.J. Li, X. Fang, B. Bucher et al., Modified astrophysical S-factor of $^{12}C+^{12}C$ fusion reaction at sub-barrier energies. Chin. Phys. C **44**, 115001 (2020). https://doi.org/10.1088/1674-1137/abae56
15. B. Bucher, X.D. Tang, X. Fang et al., First direct measurement of $^{12}C(^{12}C, n)^{23}Mg$ at stellar energies. Phys. Rev. C. **114**, 251102 (2015). https://doi.org/10.1103/PhysRevLett.114.251102
16. J. Zickefoose, A. Di Leva, F. Strieder et al., Measurement of the $^{12}C(^{12}C, p)^{23}Na$ cross section near the Gamow energy. Phys. Rev. C. **97**, 065806 (2018). https://doi.org/10.1103/PhysRevC.97.065806
17. J.R. Patterson, H. Winkler, C.S. Zaidins, Experimental investigation of the stellar nuclear reaction $^{12}C + ^{12}C$ at low energies. Astrophys. J. **157**, 367 (1969). https://doi.org/10.1086/150073
18. H.W. Becker, K.U. Kettner, C. Rolfs et al., The $^{12}C + ^{12}C$ reaction at subcoulomb energies. Z. Phys. A **303**, 305–312 (1981). https://doi.org/10.1007/BF01421528

19. M.G. Mazarakis, W.E. Stephens, Experimental measurements of the $^{12}C+^{12}C$ nuclear reactions at low energies. Phys. Rev. C. **7**, 1280–1287 (1973). https://doi.org/10.1103/PhysRevC.7.1280
20. T. Spillane, F. Raiola, C. Rolfs et al., $^{12}C+^{12}C$ fusion reactions near the Gamow energy. Phys. Rev. Lett. **98**, 122501 (2007). https://doi.org/10.1103/PhysRevLett.98.122501
21. M.D. High, B. Čujec, The $^{12}C+^{12}C$ sub-coulomb fusion cross section. Nucl. Phys. A **282**, 181–188 (1977). https://doi.org/10.1016/0375-9474(77)90179-8
22. G. Fruet, S. Courtin, M. Heine et al., Advances in the direct study of carbon burning in massive stars. Phys. Rev. Lett. **124**, 192701 (2020). https://doi.org/10.1103/PhysRevLett.124.192701
23. W.P. Tan, A. Boeltzig, C. Dulal et al., New measurement of $^{12}C+^{12}C$ fusion reaction at astrophysical energies. Phys. Rev. Lett. **124**, 192702 (2020). https://doi.org/10.1103/PhysRevLett.124.192702
24. P. Prati, On behalf of the LUNA collaboration, the LUNA-MV facility at Gran Sasso. J. Phys. Conf. Ser. **1342**, 012088 (2020). https://doi.org/10.1088/1742-6596/1342/1/012088
25. Y.T. Li, W.P. Lin, B.S. Gao et al., Development of a low-background neutron detector array. Nucl. Sci. Tech. **33**, 41 (2022). https://doi.org/10.1007/s41365-022-01030-0
26. W.P. Liu, Z.H. Li, J.J. He et al., Progress of underground nuclear astrophysics experiment JUNA in China. Few-Body Syst. **63**, 43 (2022). https://doi.org/10.1007/s00601-022-01735-3
27. Y.J. Chen, L.Y. Zhang, Examining the fluorine overabundance problem by conducting Jinping deep underground experiment. Nucl. Tech. **46**, 110501 (2023). https://doi.org/10.11889/j.0253-3219.2023.hjs.46.110501. (**in Chinese**)
28. J.Y.H. Li, Y.J. Li, Z.H. Li et al., Nuclear astrophysics research based on HI-13 tandem accelerator. Nucl. Tech. **46**, 080002 (2023). https://doi.org/10.11889/j.0253-3219.2023.hjs.46.080002. (**in Chinese**)
29. L. Morales-Gallegos, M. Aliotta, L. Gialanella et al., Direct measurements of the $^{12}C+^{12}C$ reactions cross-sections towards astrophysical energies. Eur. Phys. J. A **60**, 11 (2024). https://doi.org/10.1140/epja/s10050-024-01233-6
30. Z.C. Zhang, X.Y. Wang, T.L. Pu et al., Studying the heavy-ion fusion reactions at stellar energies using time projection chamber. Nucl. Instrum. Meth. A **1016**, 165740 (2021). https://doi.org/10.1016/j.nima.2021.165740
31. J. Zickefoose, J. Schweitzer, T. Spillane et al., Low energy beam induced background studies for a $^{12}C(^{12}C,p)^{23}Na$ reaction cross section measurement. In *Nuclei in the Cosmos*, 19 (2010). http://adsabs.harvard.edu/abs/2010nuco.confE..19Z
32. L. Morales-Gallegos, M. Aliotta, C.G. Bruno et al., Reduction of deuterium content in carbon targets for $^{12}C+^{12}C$ reaction studies of astrophysical interest. Eur. Phys. J. A **54**, 132 (2018). https://doi.org/10.1140/epja/i2018-12564-8
33. X.Y. Wang, N.T. Zhang, Z.C. Zhang et al., Studies of the 2α and 3α channels of the $^{12}C+^{12}C$ reaction in the range of E_{cm}=8.9 MeV to 21 MeV using the active target time projection chamber. Chin. Phys. C **46**, 104001 (2022). https://doi.org/10.1088/1674-1137/ac7a1d
34. X.B. Li, L.H. Ru, Z.C. Zhang et al., Construction and performance test of charged particle detector array for MATE. Nucl. Sci. Tech. **35**, 131 (2024). https://doi.org/10.1007/s41365-024-01500-7
35. Y.H. Zhai, Y. Yang, L.T. Sun et al., Production of high intensity highly charged cocktail beams at LEAF. Nucl. Instrum. Meth. A **1027**, 166157 (2022). https://doi.org/10.1016/j.nima.2021.166157
36. Q. Liu, H.B. Liu, S. Chen et al., A successful application of thinner-THGEMs. J. Instrum. **8**, C11008–C11008 (2013). https://doi.org/10.1088/1748-0221/8/11/c11008
37. J.X. Feng, Z.Y. Zhang, J.B. Liu et al., A thermal bonding method for manufacturing micromegas detectors. Nucl. Instrum. Meth. A **989**, 164958 (2021). https://doi.org/10.1016/j.nima.2020.164958
38. J.X. Feng, Z.Y. Zhang, J.B. Liu et al., A novel resistive anode using a germanium film for Micromegas detectors. Nucl. Instrum. Method A **1031**, 166595 (2022). https://doi.org/10.1016/j.nima.2022.166595
39. H.Y. Du, C.B. Du, K. Han et al., A gaseous time projection chamber with Micromegas readout for low-radioactive material screening. Radiat. Detect. Technol. Methods **7**, 90–99 (2023). https://doi.org/10.1007/s41605-022-00364-y
40. Z. Khalaj, M. Ghoranneviss, E. Vaghri et al., Diamond and diamond-like carbon, in *Diamond and Related Nanostructures*. ed. by M.V. Diudea, C.L. Nagy (Springer, Dordrecht, 2013), pp.29–47
41. L. Zhong, L.J. Guo, J.C. Wang et al., Excellent heat transfer and mechanical properties of graphite material with rolled-up graphene layers. Carbon **208**, 123–130 (2023). https://doi.org/10.1016/j.carbon.2023.03.041
42. Y. Zhou, Y. Wang, Q. Lei et al., Nanostructures and nanomechanical properties of ion-irradiated HOPG. Carbon Lett. **31**, 593–599 (2021). https://doi.org/10.1007/s42823-020-00183-5
43. X.D. Tang, S.B. Ma, X. Fang et al., An efficient method for mapping the $^{12}C+^{12}C$ molecular resonances at low energies. Nucl. Sci. Tech. **30**, 126 (2019). https://doi.org/10.1007/s41365-019-0652-9
44. J.F. Ziegler, Website. www.srim.org (Accessed February 2014)
45. W.P. Tan, A. Gula, K. Lee et al., Coincident measurement of the ^{12}C-^{12}C fusion cross section via the differential thick-target technique. Phys. Rev. C (2024). https://doi.org/10.1103/PhysRevC.110.035808
46. G.J. Feldman, R.D. Cousins, Unified approach to the classical statistical analysis of small signals. Phys. Rev. D **57**, 3873 (1988). https://doi.org/10.1103/PhysRevD.57.3873